Journal of Sustainable Metallurgy (2024) 10:1141–1155
https://doi.org/10.1007/s40831-024-00873-8

THEMATIC SECTION: REACTION KINETICS STUDY OF FERROUS AND NON-FERROUS MATERIALS USING HYDROGEN AND BIOMASS

Microstructural Investigation of Discarded NdFeB Magnets After Low-Temperature Hydrogenation

Alireza Habibzadeh[1] · Mehmet Ali Kucuker[2] · Öznur Çakır[3,4] · Mertol Gökelma[1]

Received: 15 February 2024 / Accepted: 16 June 2024 / Published online: 26 June 2024

Abstract

Due to continuously increasing demand and limited resources of rare-earth elements (REEs), new solutions are being sought to overcome the supply risk of REEs. To mitigate the supply risk of REEs, much attention has recently been paid to recycling. Despite the more common recycling methods, including hydrometallurgical and pyrometallurgical processes, hydrogen processing of magnetic scrap (HPMS) is still in the development stage. Magnet-to-magnet recycling via hydrogenation of discarded NdFeB magnets provides a fine powder suitable for the production of new magnets from secondary sources. One of the crucial aspects of HPMS is the degree of recovery of the magnetic properties, as the yield efficiency can easily reach over 95%. The amount, morphology, and distribution of the Nd-rich phase are the key parameters to achieve the excellent performance of the magnet by isolating the matrix grain. Therefore, a better insight into the microstructure of the matrix grains and the Nd-rich phase before and after hydrogenation is essential. In this study, a low-temperature hydrogenation process in the range of room temperature to 400 °C was conducted as the first step to recycle NdFeB magnets from discarded hard disk drives (HDDs), and the hydrogenated powder was characterized by electron microscopy and X-ray diffraction. The results show that there are three different morphologies of the Nd-rich phase, which undergo two different transformations through oxidation and hydride formation. While at lower temperatures (below 250 °C) the degree of pulverization is higher and the experimental evidence of hydride formation is less clear, at higher temperatures the degree of pulverization decreases. The formation of neodymium hydride at higher temperatures prevents further oxidation of the Nd-rich phase due to its high stability.

The contributing editor for this article was Xuefeng Dong.

✉ Alireza Habibzadeh
alirezahabibzadeh@iyte.edu.tr

[1] Department of Materials Science and Engineering, İzmir Institute of Technology, 35433 Izmir, Türkiye

[2] Department of Environmental Engineering, İzmir Institute of Technology, 35433 Izmir, Türkiye

[3] Turkish Energy, Nuclear and Mineral Research Agency (TENMAK), Rare Earth Elements Research Institute (NATEN), 06980 Ankara, Türkiye

[4] Department of Metallurgical and Materials Engineering, Yildiz Technical University, 34220 Istanbul, Türkiye

Graphical Abstract

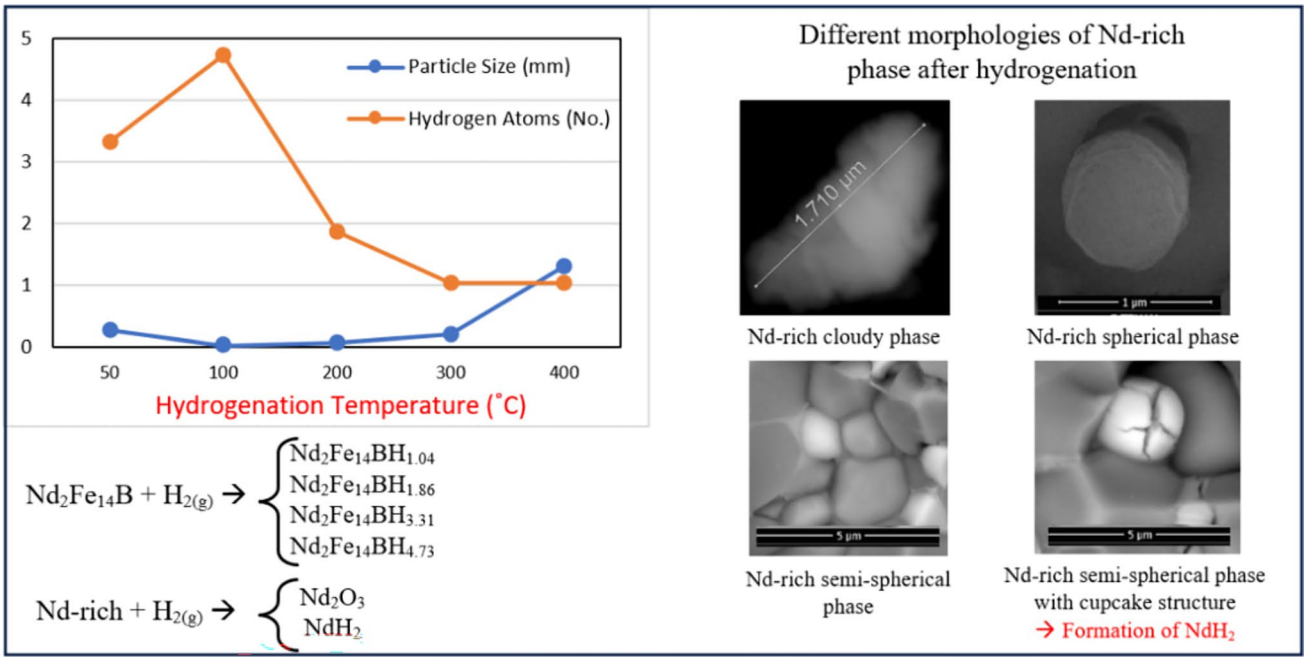

Keywords Hydrogen decrepitation · Magnet-to-magnet recycling · Nd-rich phase · HPMS

Introduction

Introduced in the 1980s, sintered neodymium-iron-boron (NdFeB) permanent magnets are used in a variety of applications due to their excellent magnetic properties [1]. The excellent performance of the NdFeB magnets is attributed to its microstructure, in which the tetragonal $Nd_2Fe_{14}B$ grains (φ-phase) are surrounded and isolated by the Nd-rich grain boundary phase (intergranular) [2, 3]. The Nd-rich phase, resulting from additional Nd during manufacturing, forms a thin, continuous layer around matrix grains, preventing reverse magnetic domain nucleation through core–shell structures [4–6]. The wetting and penetration of the Nd-rich grain boundary phase between matrix grains, crucial for optimal magnet performance, are significantly influenced by the initial chemical composition [7]. Notably, the Nd content in the magnet strongly affects Nd presence in the Nd-rich phase; reducing the initial Nd content from 15 to 12% decreases Nd content in the Nd-rich grain boundary phase from 80 to 30% [8]. Moreover, the inclusion of alloying elements like Dy and Tb, typically added in hydride form (DyH_3 and TbH_2), results in a single or double-layer core–shell structure, enhancing magnetic isolation of matrix grains leading to an increase in the performance of the magnet [9, 10].

The permanent magnet industry, which mainly relies on NdFeB rather than samarium–cobalt (Sm–Co) magnets due to the high price and rarity of Sm and the avoidance of the use of strategic Co metal, consumes around 23% of all REEs produced worldwide [11, 12]. The ever-increasing demand and necessity of REEs for the development of the renewable energy industry and electromobility have led to these materials being at the top of the list of critical raw materials (CRMs) worldwide [13–15]. Therefore, recycling discarded NdFeB permanent magnets containing Nd, Pr, Dy, Gd, and Tb has recently attracted much attention to alleviate the supply risk. However, it is still in the development stage, and there is no established industrial process [16]. Standard methods for the recovery of REEs from discarded NdFeB magnets include pyrometallurgical routes such as electroslag refining, liquid metal extraction, and direct remelting or hydrometallurgical routes such as direct leaching in mineral acids, leaching with oxidative roasting, leaching with chlorination roasting and bioleaching [13, 17, 18]. All of these recycling processes focus on the recovery of elemental rare earth through the production of rare-earth oxides and the subsequent energy-intensive molten salt electrolysis step.

However, hydrogen processing of magnetic scrap (HPMS) focuses on magnet-to-magnet recycling, skipping some energy-intensive steps with high environmental

impact and achieving an efficiency of over 90% [4, 19]. HPMS, which has recently attracted much attention, is carried out using both low-temperature (hydrogen decrepitation (HD)) and high-temperature (hydrogenation disproportionation desorption and recombination (HDDR)) processes [4]. It is believed that low-temperature hydrogenation (HD), relies mainly on the formation of NdH_x from the Nd-rich grain boundary phase and pulverization due to the local expansion between the matrix grains, which leads to the collapse of the entire structure of the magnet [20]. With subsequent processing, including pressing, aligning, vacuum sintering, coating, and magnetizing, the obtained powder can be directly used to produce new sintered magnets [21].

The mechanism of hydrogen decrepitation at the microstructural level is based on the high diffusivity of hydrogen atoms that penetrate into the Nd-rich grain boundary phase and the interstitial sites of the $Nd_2Fe_{14}B$ matrix grains (φ-phase), leading to the formation of NdH_x and $Nd_2Fe_{14}BH_x$ [12, 22]. In contrast to the assumption that the formation of $Nd_2Fe_{14}BH_x$ cannot prevent oxidation of the produced powder in the ambient atmosphere [23], it is proved that the formation of NdH_x can protect the Nd-rich phase from oxidation due to its high stability, which is crucial for the recovery of magnetic properties in the final stage of magnet-to-magnet recycling [24]. Since the final magnetic properties of recycled NdFeB magnets strongly depend on the microstructure and the distribution of the Nd-rich phase, microstructural investigation of the hydrogenated powder is required [25].

To gain a better understanding, various experimental studies have been carried out in recent decades to determine the crystal structure, chemical composition, and morphology of the Nd-rich grain boundary phase. The Nd-rich grain boundary phase consists mainly of Nd (always accompanied by Pr), some Fe, O, and some traces of B [26–28]. As a result, various microstructures and crystal structures of the Nd-rich grain boundary phase have been described, including amorphous, cubic, and hexagonal [29–31]. The amorphous Nd-rich grain boundary phase has been observed when the boundary thickness is less than 3 μm and transitions to the crystalline form as the boundary thickness increases [32, 33]. Mo et al. [26] reported that the complexity of the crystal structure of the Nd-rich phase is due to the oxygen content, and when the oxygen content is increased the crystal structure of the Nd-rich phase changes from double close-packed hexagonal (DHCP) to face-centered cubic (FCC) and finally to close-packed hexagonal (HCP) [34, 35]. Also, the reported structure of metallic Nd is DHCP, which is believed to transform into FCC during the sintering process at elevated temperatures (above 1000 °C) by absorbing more oxygen, increasing from 0.017 to 0.63 wt.% after sintering [26, 27].

The mechanism and effects of low-temperature hydrogenation in NdFeB magnets, based on experimental evidence, are still not clearly described. This work attempts to present a study on microstructural characterization of the matrix grain and the Nd-rich grain boundary phase to identify the morphologies, chemical composition, and phase transformations after low-temperature hydrogenation in the range of 25 to 400 °C.

Experimental Procedure

All discarded NdFeB magnets used in this research study were taken from discarded hard disk drives (HDDs) of the same model and brand manufactured between 2010 and 2014. The HDDs were manually disassembled to extract clean and unoxidized magnets. All magnet samples weighing 16.497 ± 0.054 g and 4.5 mm thick were peeled off (decoated) by hand to separate the Ni–Cu coating to provide a free surface for hydrogen diffusion and prevent nickel from mixing with the final hydrogenated powder [19, 36]. In the first part of the study, two samples of NdFeB magnets were broken with a hammer to prepare a cross section for electron microscopy. They were milled to prepare powders for X-ray diffraction analysis and inductively coupled plasma mass spectrometry (ICP-MS) *before hydrogenation*. In a further step, other samples of the NdFeB magnet were hydrogenated for two hours at different temperatures and then characterized by electron microscopy, X-ray diffraction, and particle size analysis to evaluate the microstructural changes *after hydrogenation*.

The experimental setup for hydrogenation shown in Fig. 1 is a stainless-steel reactor with a volume of about 3 L (the volume fraction of the sample in the reactor is 0.00073), which consists of the gas inlet, the gas outlet, a water cooling system, a vacuum gage, a pressure gage, and a place to attach a thermocouple for continuous temperature measurement. The reactor was designed so that it can be installed in a heat-resistant furnace with the lowest heat loss.

After putting the sample inside the reactor, the gas outlet was connected to a vacuum pump to evacuate the inner atmosphere of the reactor. Then it was filled with hydrogen to remove as much oxygen as possible, and this was repeated three times. A digital thermocouple continuously monitored the temperature inside the reactor. After reaching the targeted temperatures (in the range of 25–400 °C), the hydrogen gas was blown into the reactor for 2 h at a flow rate of 1 l/min. After hydrogenation was completed, the reactor was removed from the furnace, and argon was purged into the reactor until it had reached room temperature.

The product powder was then immediately transferred to the glovebox for sampling. The atmosphere in the glovebox contains less than 50 ppm of oxygen and a moisture

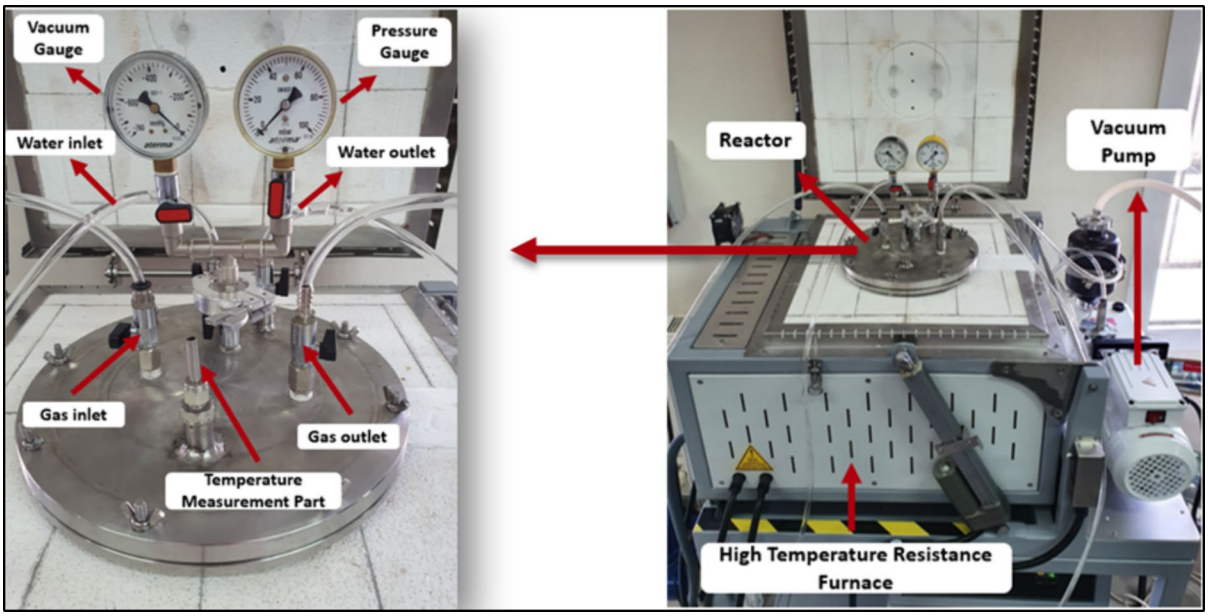

Fig. 1 Experimental setup for hydrogenation of discarded NdFeB magnets

Table 1 The initial chemical composition of the NdFeB magnet extracted from a discarded HDD, obtained by ICP-MS

Element	Fe	Nd	Pr	B	Co	Ni	Cr	Cu	Dy	Gd
wt.%	67.5	23.33	3.87	1.01	0.75	0.31	0.11	0.11	1.08	0.885

content of less than 100 ppm. Under the glovebox, manual sieving was performed as needed to separate large particles (only for samples hydrogenated at 400 °C). Finally, the collected samples were characterized by X-ray diffraction, scanning electron microscopy with energy dispersive spectroscopy (SEM–EDS), and particle size analysis to determine the effects of hydrogenation temperature. The focus was on the identification of different phases and their distribution, morphology, chemical composition, and oxygen content. In addition, ImageJ software was used to measure the length of transgranular cracks observed in the SEM images.

Results and Discussion

The initial chemical composition of the NdFeB magnets which were extracted from the HDDs, is tabulated in Table 1. This result shows that around 27 wt.% of the magnet is composed of REEs which is enough to form a continuous Nd-rich layer between the matrix grain. In the following sections, the matrix grain and Nd-rich grain boundary phases were studied before and after hydrogenation.

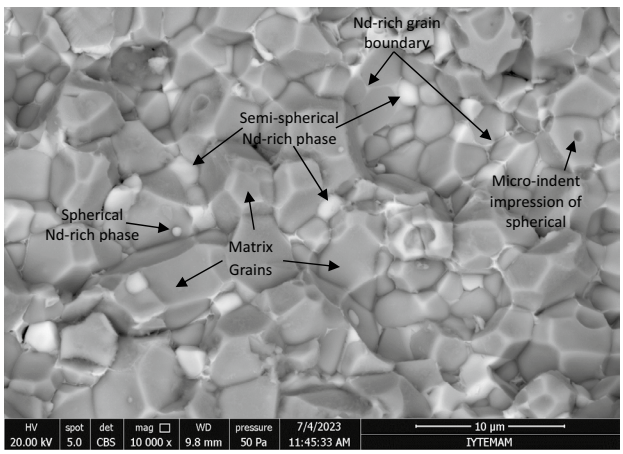

Fig. 2 Cross-sectional BSE-SEM image of all phases of discarded NdFeB magnet before hydrogenation

$Nd_2Fe_{14}B$ Matrix Grains

Before Hydrogenation

Figure 2 shows the backscattered electron (BSE) SEM image of the cross section of the discarded NdFeB magnet. In this figure, the $Nd_2Fe_{14}B$ matrix grains, spherical Nd-rich phase,

micro-indent impression caused by spherical Nd-rich phase, semi-spherical Nd-rich phase, and the Nd-rich grain boundary phase have been observed. However, only the matrix grains will be studied in this section and the rest will be discussed in the following. Figure 2 shows that the matrix grains of $Nd_2Fe_{14}B$ (φ phase) are found in different grain sizes ranging from 2 to 8 µm. Table 2 shows the average chemical composition of the $Nd_2Fe_{14}B$ matrix grain (wt.%) before and after low-temperature hydrogenation obtained by EDS point analysis. Based on the EDS results, the matrix grains contain, on average, about 67 ± 4.02% Fe, 25 ± 0.69% Nd, 6 ± 0.24% Pr, and 1% B without considering the oxygen absorption. The low oxygen absorption of the matrix grains during hydrogenation up to 400 °C confirms that the matrix grain is far more resistant to oxidation than the Nd-rich phases. This can be attributed to the fact that the tetragonal structure of $Nd_2Fe_{14}B$ offers less favorable sites for oxygen absorption due to its higher density compared to the Nd-rich phase. Moreover, due to the low presence of oxygen in the system and the higher reactivity of the Nd-rich phase, most of the oxygen could be absorbed by this phase. In addition, kinetic effects such as slower diffusion rates and longer reaction times could also contribute to the observed lower degree of oxidation in the $Nd_2Fe_{14}B$ phase compared to the Nd-rich phase. Another observation is that Pr appears to always accompany Nd, and the average ratio of Pr/Nd in the matrix grain is 0.201 ± 0.013.

Figure 3 represents the X-ray diffraction of the discarded NdFeB magnet. The $Nd_2Fe_{14}B$ matrix grain and some traces of neodymium oxide (Nd_2O_3) were detected by diffraction. The presence of neodymium oxide might be due to the high reactivity of Nd and the duration of exposure to air after decoating and milling for sample preparation.

After Hydrogenation

Figures 4 and 5 show the X-ray diffraction results after low-temperature hydrogenation in the range of 25–400 °C, depicting the formation of four different hydrides of the matrix grains, namely $Nd_2Fe_{14}BH_{1.04}$, $Nd_2Fe_{14}BH_{1.86}$, $Nd_2Fe_{14}BH_{3.31}$, and $Nd_2Fe_{14}BH_{4.73}$, along with unreacted $Nd_2Fe_{14}B$ matrix grain, neodymium oxide (Nd_2O_3), and hydride (NdH_2). These results show that the hydrogen absorption by the matrix grains varies at different temperatures. First, by increasing the hydrogenation temperature from 25 to 100 °C, the dominant phase changes from a mixture of $Nd_2Fe_{14}BH_{3.31}$ and $Nd_2Fe_{14}BH_{4.73}$ to the latter with maximum hydrogen content. Then by further increasing the temperature, the $Nd_2Fe_{14}B$ hydride with a lower index of hydrogen was identified as the dominant phase. The $Nd_2Fe_{14}BH_{1.86}$ is the dominant phase at 200 and 250 °C, and the $Nd_2Fe_{14}BH_{1.04}$ is the dominant phase by hydrogenation above 300 °C.

The $Nd_2Fe_{14}B$ is converted to $Nd_2Fe_{14}BH_x$, where x is a function of temperature but with two opposite trends. First, the value of x in the dominant phase increases from 3.31 to 4.73 when the temperature rises from 25 to 100 °C, and then decreases to 1.04 when the temperature is further increased to 400 °C, showing that hydrogen absorption is highest at 100 °C. This result is also in agreement with

Table 2 Chemical composition (wt.%) of $Nd_2Fe_{14}B$ matrix grain before and after low-temperature hydrogenation of NdFeB magnets, obtained by EDS point analysis

Elements	Before HD	HD at 100 °C	HD at 200 °C	HD at 300 °C	HD at 400°C
B	0.00	1.04 ± 1.79	2.39	0.06 ± 0.14	0.00
O	3.42 ± 3.48	2.22 ± 1.09	2.14	1.12 ± 1.26	3.90
Fe	65.62 ± 3.94	66.65 ± 2.98	67.85	68.73 ± 1.49	67.18
Pr	5.32 ± 0.22	5.05 ± 0.61	4.48	4.91 ± 0.37	4.81
Nd	25.65 ± 0.64	25.04 ± 1.77	23.13	25.18 ± 2.23	24.12
Dy	0.00	0.00	0.00	0.00	0.00

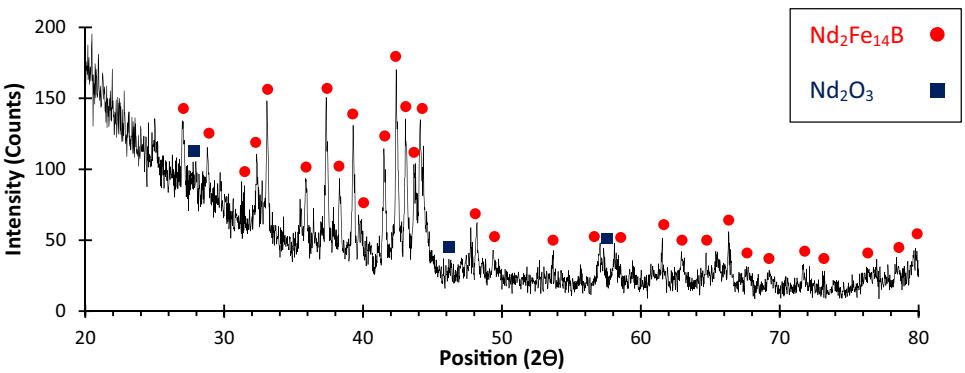

Fig. 3 X-ray diffraction pattern of the discarded NdFeB magnet before hydrogenation

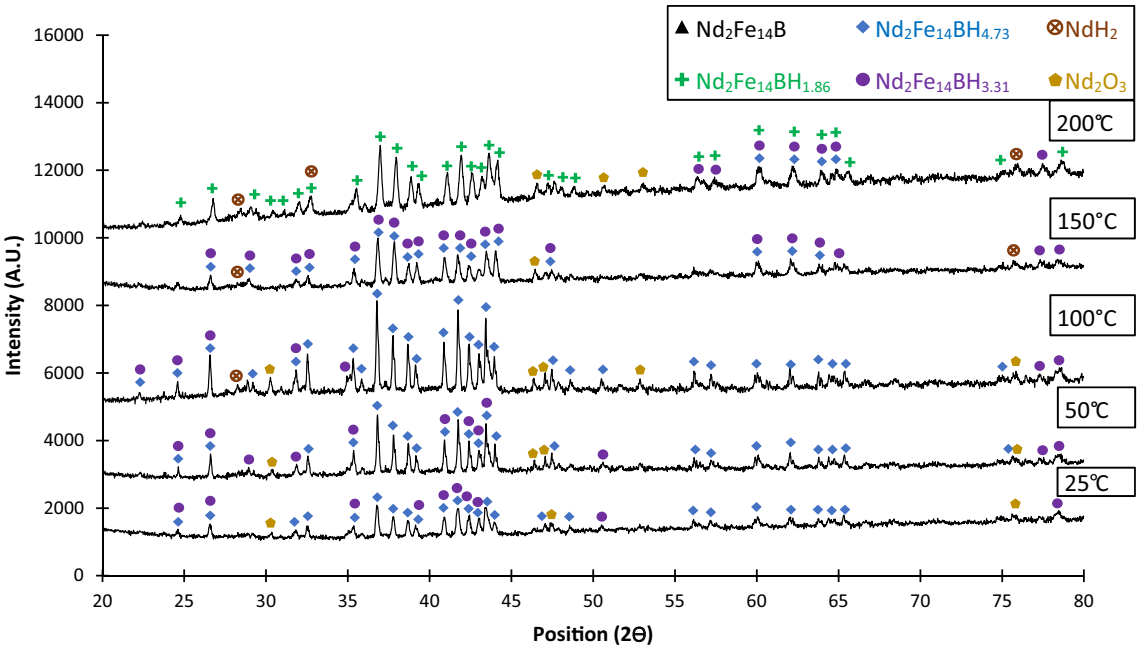

Fig. 4 X-ray diffraction patterns after hydrogenation of discarded NdFeB magnets in the range of 25–200 °C

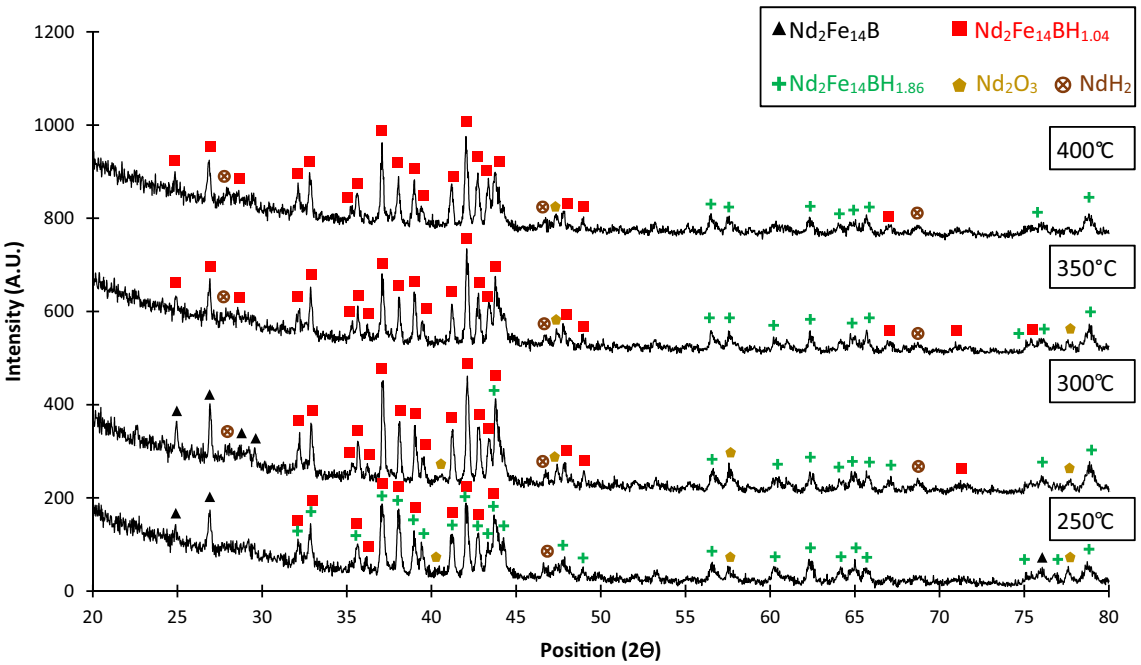

Fig. 5 X-ray diffraction patterns after hydrogenation of discarded NdFeB magnets in the range of 250–400 °C

Michalsky et al. [21], who reported the highest hydrogen uptake by hydrogenation at 100 °C. A hydrogenation temperature of 200 °C is the cut-off point, and below that (Fig. 4), $Nd_2Fe_{14}BH_{1.04}$ and $Nd_2Fe_{14}BH_{1.86}$ and above that (Fig. 5) $Nd_2Fe_{14}BH_{3.31}$ and $Nd_2Fe_{14}BH_{4.73}$ cannot be detected, respectively.

This result can be attributed to the increase in hydrogen diffusivity with increasing temperature [37]. When the hydrogenation temperature is increased up to 100 °C, the hydrogen atoms have sufficient diffusivity and mobility to fully penetrate into the tetrahedral interstitial sites of the $Nd_2Fe_{14}B$ unit cell and form a strong bond with Nd [22,

38]. The formation of hydride with a lower hydrogen content above 100 °C can be explained in two ways. First, as reported by Wirth et al. [39], it could be due to the surface barrier energy (U_s). The 'surface barrier' refers to the resistance encountered by hydrogen atoms when they first come into contact with the surface of the material. This barrier can slow down the initial entry of hydrogen atoms into the material. At higher temperatures, the increased energy of the hydrogen atoms allows them to overcome this barrier more easily, leading to faster and more efficient hydrogen diffusion into the bulk of the material [40, 41]. It means at a lower temperature, the diffusion is the slowest step in the process and controls the kinetics, while by increasing the temperature above 100 °C the particle flux through the surface is a slower step. In fact, the particle flux through the surface barrier is smaller than the possible diffusion flux under the surface layer. After surface absorption of the hydrogen and forming hydride at the solid–gas interface, it can act as a passive or protective layer from further hydrogenation. The second explanation is based on the classical jumping mechanism, which states that the diffusion of hydrogen atoms is determined by the rate at which the atoms hop between interstitial lattice sites, which is a function of temperature [37]. Suppose the diffusivity and mobility of hydrogen atoms are further increased. In this case, the residence time in the interstitial sites decreases because of an increase in hopping between interstitial sites, which could result in leaving a $Nd_2Fe_{14}B$ unit cell with lower hydrogen content. Overall, it seems the kinetics of the reaction is under control by the surface-substrate interface and the first explanation is more likely.

Figure 6 illustrates the median particle size (D50) of the powder obtained after low-temperature hydrogenation in the range of 25–400 °C. The size of the grouped particles (or non-detached agglomerates) initially decreased to its minimum (33 µm) when the hydrogenation temperature was increased to 100 °C, and then remained in the lowest range when the temperature was further increased to 200 °C. When the hydrogenation temperature was increased above 200 °C, the median particle size increased to 1220 µm. A higher hydrogen content is expected for the samples with a lower particle size due to better embrittlement. Therefore, the particle size analysis supports the X-ray diffraction results indicating the smallest particle size is reached when the hydrogenation temperatures are between 100 and 200 °C, which favors the formation of $Nd_2Fe_{14}BH_{4.73}$ with the highest hydrogen content. It can be concluded that the highest hydrogen uptake leads to a stronger local expansion, resulting in the lowest particle size in the range of 33 to 51 µm. At temperatures below 100 °C, the average particle size is about eight times bigger than at 100–200 °C due to the lack of sufficient mobility and diffusivity of the hydrogen atoms. While the mobility of hydrogen atoms increases significantly with increasing temperature in the range from 100 to 400 °C, the opposite trend is evident for particle size. The drastic increase in particle size above 200 °C can be attributed to the reaction kinetics and surface barrier energy which leads to the formation of $Nd_2Fe_{14}BH_x$ with lower hydrogen content, as well as crack formation and propagation, which will be discussed in the following.

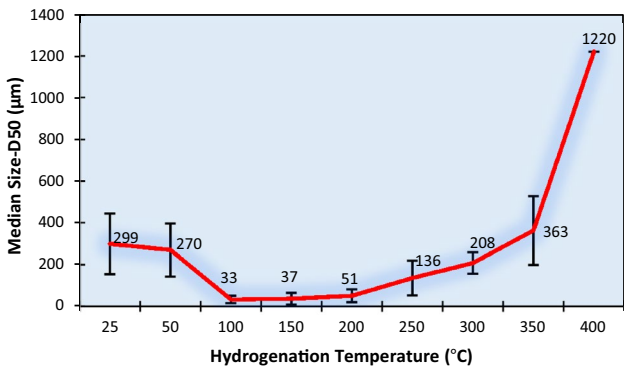

Fig. 6 Median particle size (D50) ($\alpha = 0.05$) of the obtained powder after hydrogenation of discarded NdFeB magnets

Figure 7 shows the BSE-SEM images of the intergranular and transgranular cracks in the matrix grain as a result of hydrogenation, which were also observed by Kilner et al. [42]. Intergranular cracks are widespread and form the basis for pulverization. Two different types of transgranular cracks can be seen in Fig. 7, including an enclosed crack that occurs within the matrix grain without reaching the edges of the grain (Fig. 7a), and the edge-to-edge transgranular cracks that cut through the grains (Fig. 7c).

At lower temperatures, the enclosed transgranular cracks were observed in direct contact with the micro-indent impression of the Nd-rich spherical phase (Fig. 7a) or close to the spherical phase itself (Fig. 7b). As explained in Sect. "Spherical Nd-Rich Phase," the spherical phase could cause an additional force for crack initiation since the activation energy for crack initiation and propagation cannot be overcome at a lower temperature. However, at temperatures above 200 ˚C, there are almost no trapped transgranular cracks as the energy for crack initiation and propagation can be overcome by the higher mobility of atoms and imperfections (Fig. 7c, d).

Table 3 shows the result of data mining using ImageJ software from nearly 300 SEM images, tabulating the scanned area, the number of transgranular cracks counted in the area unit, the average length of transgranular cracks, the longest transgranular crack detected, and the status of the transgranular crack with respect to the connection to the intergranular crack. When the temperature is increased to 200 °C, the number of transgranular cracks increases dramatically to more than 300 in square millimeters and then

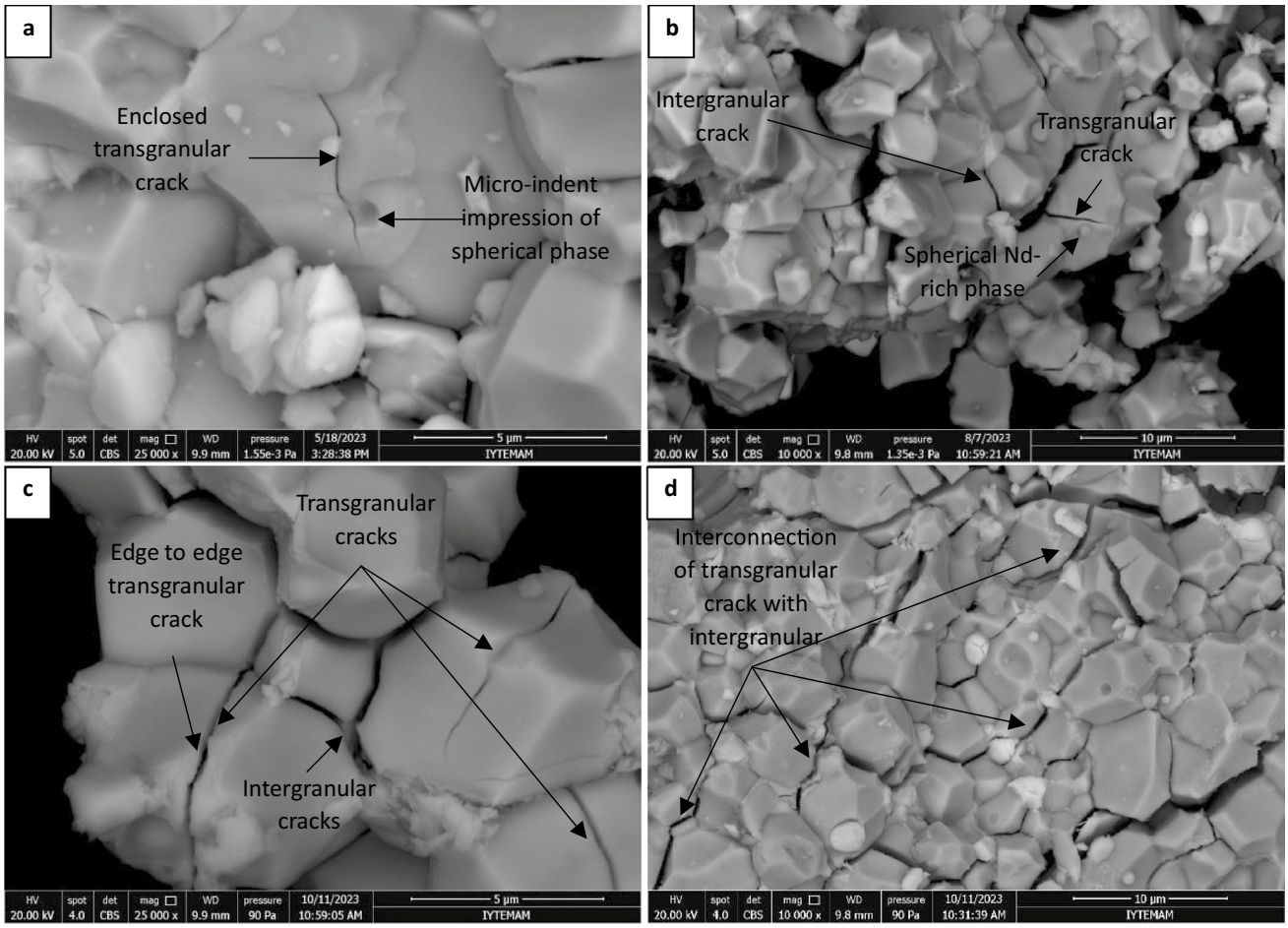

Fig. 7 BSE-SEM images of intergranular and transgranular cracks, spherical Nd-rich phase, and micro-indent impression of spherical phase in the matrix grain of $Nd_2Fe_{14}B$ after hydrogenation at **a** 50 °C, **b** 100 °C, **c** 250 °C, and **d** 400 °C

Table 3 Transgranular crack length and its distribution in the microstructure using ImageJ

Hydrogenation Temperature	25 °C	50 °C	100 °C	150 °C	200 °C	250 °C	300 °C	350 °C	400 °C
Total scanned area (mm^2)	~0.24	~0.34	~0.67	~0.23	~0.13	~0.23	~0.14	~0.25	~0.24
Number of cracks in 1 mm^2	0	~30	~64	~142	~303	~230	~295	~212	~245
Average crack length (μm)	0	3.67 ± 1.17	4.59 ± 0.83	5.84 ± 1.18	5.03 ± 0.86	4.95 ± 1.02	5.53 ± 0.99	5.78 ± 1.03	5.97 ± 1.63
Max. crack length (μm)	0	5.05	8.54	10.83	8.46	9.92	13.51	10.97	19.5
Interconnection of intergranular & transgranular cracks	None	None	Rare	Few	Often	Medium	High	High	High

fluctuates after a slight decrease between 212 and 295 when further increased to 400 °C. Although the result does not follow a linear progression, the 200 °C appears to be the saturation temperature for crack initiation, which supports pulverization and reduction in grain size. The average length of the transgranular cracks fluctuates between 4.5 and 6 μm when the temperature is increased from 100 to 400 °C after it had previously increased. However, the maximum length of the transgranular crack generally increases with increasing temperature, reaching 19.5 μm at 400 °C, due to a crack that cuts through four $Nd_2Fe_{14}B$ grains. The key point in Table 3 is that cracks propagate more easily through or between grains as temperature increases, as can be seen in Fig. 7c, where a transgranular crack continues its path between grains after cutting the other grain in two. This result shows that although the average size of the transgranular cracks does

not change significantly by increasing the temperature over 150 °C, their propagation through the microstructure is entirely influenced by the temperature. As the temperature increases, the mobility of the atoms increases so that they can overcome the activation energy for crack propagation and release the stress caused by the local expansion due to hydrogenation. This energy release leads to fracture before hydrogenation is complete. In other words, it is assumed that at lower temperatures, the lack of energy for crack initiation and propagation prevents the breakage of the mass and leads to pulverization with finer particles because of local expansion. It should be recalled that the magnet was first heated to the target temperature, and then hydrogen was blown to the reactor so that crack initiation and propagation to fracture occurred faster than pulverization. In this state, the magnet experienced energy release. So the following expansion caused by the hydrogenation cannot provide enough energy for complete pulverization, resulting in very large particles, as shown in Fig. 6. The observation of more cracks, and at the same time, a larger particle size at a higher temperature can be explained by the fact that more cracks formed at higher temperatures, but these did not spread further so that they could be detected with the SEM. In contrast, at lower hydrogenation temperatures, which result in smaller particle sizes, the cracks were initiated and propagated to the highest extent so that they could no longer be observed. Furthermore, the extent to which the matrix grain absorbs hydrogen can explain the mechanism of pulverization, as discussed in detail previously.

Nd-Rich Phase

Based on the morphology and the distribution of Nd in the BSE-SEM image of the raw magnet (Fig. 2), two different Nd-rich phases can be distinguished. The first Nd-rich phase is a spherical phase at the surface of the matrix grains and the second is an Nd-rich grain boundary network consisting of a semi-spherical Nd-rich phase at the triple junctions of the matrix grain and a thin Nd-rich grain boundary phase between the matrix grains (labeled in Fig. 2). In contrast to the latter, which forms a network of grain boundary phases that are almost interconnected, the former is smaller, separated, and differently arranged.

Spherical Nd-Rich Phase

Before Hydrogenation The small spherical particles on the surface of the matrix grains can be seen throughout the cross section of the raw magnet (labeled in Fig. 2). According to the EDS point analysis, the spherical Nd-rich phase contains about 75% Nd+Pr, the rest is iron, which absorbs about 1–2% oxygen and can leave a distinct micro-indent impression (labeled in Fig. 2) on the surface of the matrix grain. Due to its spherical shape, it could originate from the liquid phase during vacuum sintering and not be remelted during the subsequent heat treatment. Inefficient heat treatment can lead to an uneven distribution of the Nd-rich phase in the microstructure, resulting in a deterioration of the final magnetic properties. The other reason for the presence of a spherical phase can be attributed to the absence of alloying elements such as copper and aluminum. Koyama et al. [8] reported that by increasing the copper content to 0.2 wt%, complete coverage of the matrix grain can be achieved by forming a eutectic composition. By forming the eutectic composition, the melting point of the Nd-rich phase can be lowered leading to a higher degree of isolation of the matrix grains by the Nd-rich phase and, thus, to better magnetic properties.

After Hydrogenation Figure 8 shows the spherical Nd-rich phase after hydrogenation at 100 and 400 °C. These SEM images of the spherical Nd-rich phase show that this phase with a size of less than 1 µm did not undergo any changes in terms of morphology and size during low-temperature hydrogenation up to 400 °C. The higher magnification secondary electron (SE) SEM image (Fig. 8a) shows a spherical Nd-rich phase about to detach from the matrix grain. In contrast, it is fully attached in Fig. 8b. The spherical Nd-rich phase was, thus, observed in three states: first, fully attached to the surface of the matrix grain; second, detached from the matrix grain (the micro-indent-impression remained), and finally, in a position between the first and second states (Fig. 8a). This phenomenon can be directly attributed to the absorption of oxygen and hydrogen, which leads to the formation of oxide and hydride, resulting in an expansion that forces the detachment of the spherical phase. The experimental evidence for this theory, which can justify the difference between Fig. 8a and b, is shown in Table 4, namely the average chemical composition of the spherical Nd-rich phase after hydrogenation at different temperatures, where the oxygen absorption of the spherical phase after hydrogenation at 100 °C is the highest among the others. The other explanation that can be associated with this phenomenon is the difference between the coefficient of thermal expansion (CTE) of the Nd-rich phase and the matrix grain and the dependence of the CTE on the chemical composition [43], 44. This observation also confirms that there is no chemical bonding between this phase and the matrix grain. According to the SEM–EDS analysis at different temperatures, the spherical Nd-rich phase is a stable phase up to 400 °C.

Table 4 represents the average chemical composition of the spherical Nd-rich phase after hydrogenation at different temperatures measured by EDS. The result shows that the oxygen content in this phase increases at lower hydrogenation temperatures and decreases at higher hydrogenation temperatures. This upward trend can be attributed to

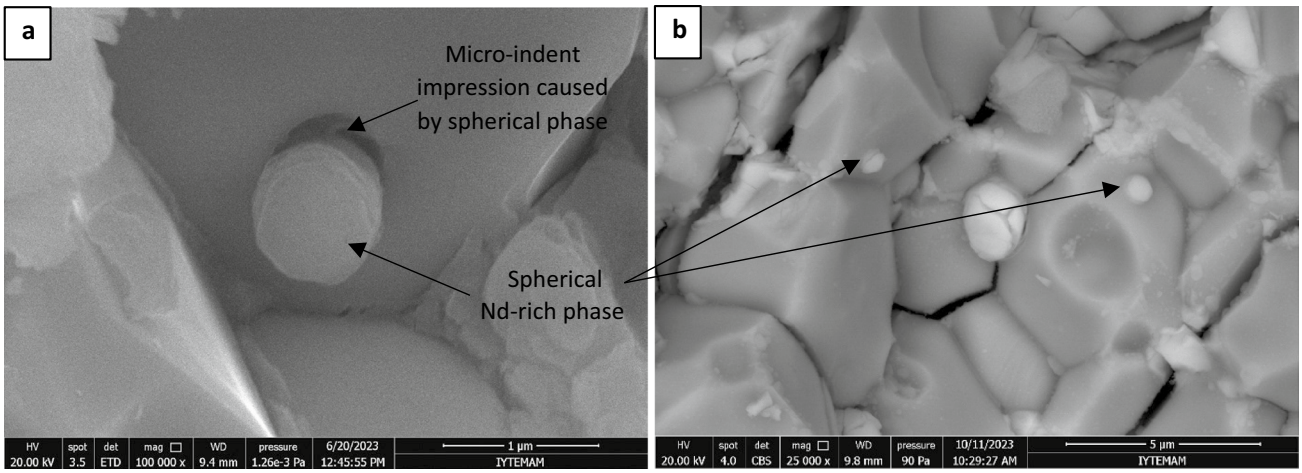

Fig. 8 SEM images of the spherical Nd-rich phase at the surface of matrix grains after hydrogenation, **a** 100 °C (SE-SEM), and **b** 400 °C (BSE-SEM)

Table 4 Average chemical composition (wt.%) of spherical Nd-rich phase before and after low-temperature hydrogenation of NdFeB magnets, obtained by EDS point analysis

Elements	Before HD	HD at 25 °C	HD at 100 °C	HD at 200 °C	HD at 300 °C	HD at 400 °C
O	4.83	17.31	18.64	19.75	4.68	10.22
Fe	34.90	29.31	16.70	19.06	31.52	26.01
Pr	10.04	8.42	11.78	7.70	11.97	11.41
Nd	50.23	44.96	51.82	52.87	51.49	52.36

the increased formation of neodymium hydride (NdH_2) at higher temperatures, a stable phase that reduces oxidation. The reduction in the Fe concentration by increasing the temperature can be attributed to the higher oxygen absorption of the spherical Nd-rich phase. In addition, the average ratio of Pr/Nd in the spherical Nd-rich phase is equal to 0.202 ± 0.039 which is almost the same as the matrix grains.

Grain Boundary Nd-Rich Network

Before Hydrogenation As presented in Fig. 2, the raw NdFeB magnet is composed of a discontinued grain boundary network consisting of an accumulated semi-spherical Nd-rich phase at the triple junctions of the matrix grain and an uneven distribution of a thin Nd-rich layer between the matrix grains.

After Hydrogenation Figure 9 shows the microstructure of NdFeB magnets after hydrogenation at 100 °C at various magnifications illustrating very long intergranular cracks resulting from hydrogenation leading to pulverization. No trace of a thin Nd-rich layer after hydrogenation can be seen in this image, and all the Nd in the thin grain boundary phase has been consumed to form either neodymium hydride (NdH_2) or neodymium oxide (Nd_2O3). This figure also shows an Nd-rich phase that appears in fuzzy form after hydrogenation, has no regular shape, and will be referred to as the *cloudy phase* from now on. Figure 10 represents EDS analysis and element mapping of all phases of Fig. 9. Based on the mapping, this cloudy phase has high amounts of Nd, Pr, and oxygen, indicating that this is an Nd-rich phase that absorbs high amounts of oxygen and converted to oxide. This statement is supported by the EDS point analysis shown in Table 5, which confirms that the oxygen uptake of the Nd-rich cloudy phase after hydrogenation can reach 24% at lower temperatures and decrease to about 18% at higher temperatures (above 350 °C). The lower oxidation at higher temperatures could be related to the formation of neodymium hydride. Without considering the oxygen content, the EDS results show that the Nd-rich cloudy phase contains 60–80% Nd and Pr, while the rest is up to 100% iron. Based on the reports by different researchers [26, 30, 34], the crystal structure of the Nd-rich cloudy phase can be FCC and contains neodymium oxide in the form of Nd_2O_3.

Figure 11 shows that the Nd-rich cloudy phase can be found everywhere, like debris, and even frequently in triple junctions which means that the semi-spherical phase can be converted to the cloudy phase, even by hydrogenation at 50 °C (see Fig. 11b). While the size of the Nd-rich cloudy phase in Fig. 11, a is less than 2 µm, it is about 4 µm in Fig. 11b, and in general, it can be detected in a wide size

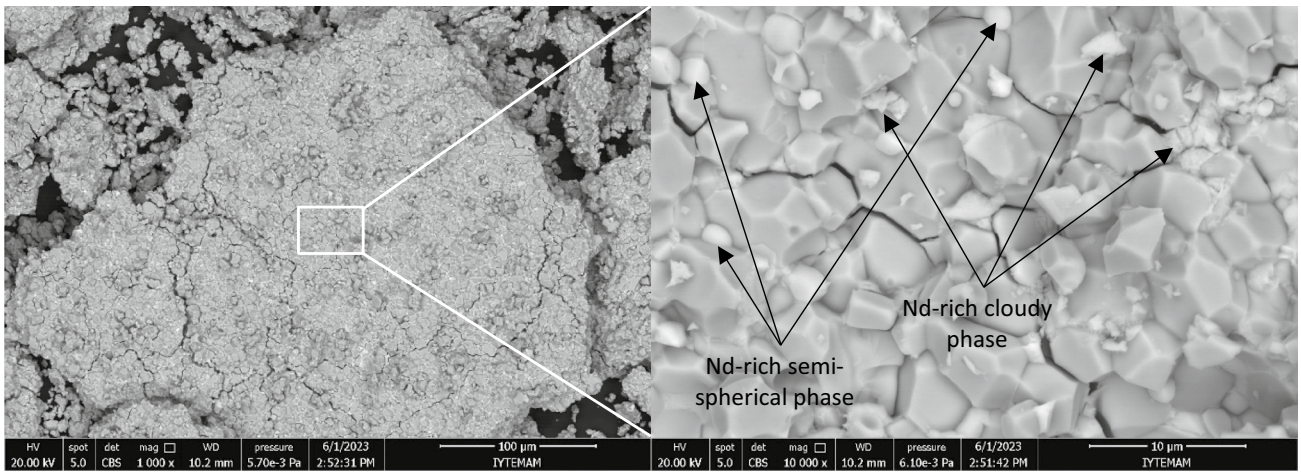

Fig. 9 BSE-SEM images of the hydrogenated magnet at 100 °C representing the Nd-rich cloudy phase

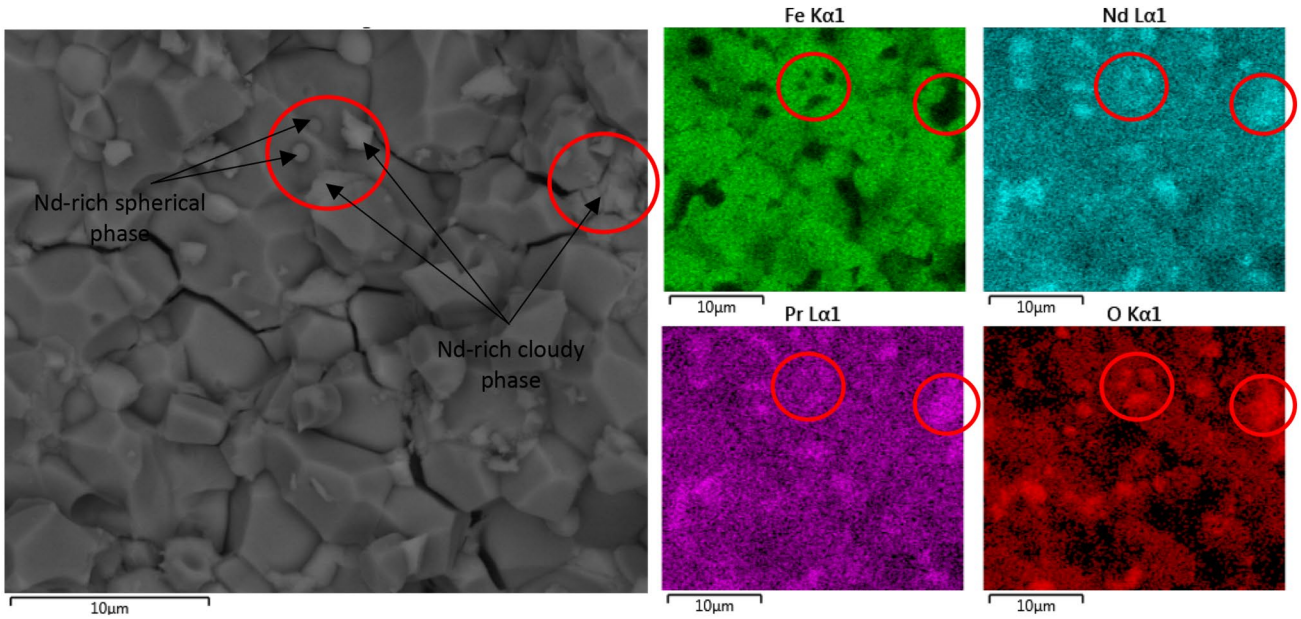

Fig. 10 BSE-SEM images and elemental mapping of a hydrogenated magnet at 100 °C

Table 5 Average chemical composition (wt.%) of Nd-rich cloudy phase after low-temperature hydrogenation obtained by EDS

Elements	HD at 25 °C	HD at 100 °C	HD at 200 °C	HD at 300 °C	HD at 400 °C
O	16.62	24.42 ± 5.04	23.34 ± 3.77	24.09 ± 2.28	18.7
Fe	13.9	15.11 ± 4.72	11.79 ± 8.45	19.79 ± 5.89	18.2
Pr	17.3	12.38 ± 2.23	13.82 ± 4.06	10.36 ± 1.41	12.19
Nd	52.18	47.94 ± 4.79	50.68 ± 5.63	45.77 ± 5.29	50.91

range, with most cases recognized as clusters, as marked by a yellow circle in Fig. 10.

The other part of the Nd-rich grain boundary network that accumulates at the triple junctions of the matrix grains, which can be seen and recognized in Figs. 2, 8, and 9, was termed the *semi-spherical Nd-rich phase*. This phase underwent two opposite pathways during hydrogenation at different temperatures. In the first pathway, which is more common at lower temperatures, the semi-spherical Nd-rich particles absorb oxygen, and the oxygen content increases

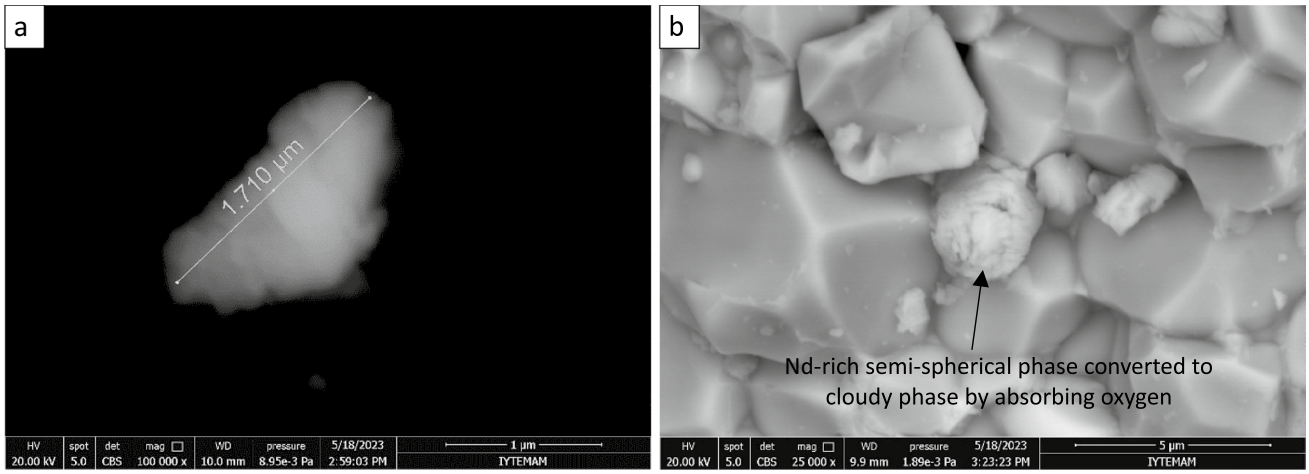

Fig. 11 BSE-SEM images of the Nd-rich cloudy phase of the hydrogenated magnet at 50 °C in two different conditions, **a** flying debris of Nd-rich cloudy phase, and **b** a former semi-spherical Nd-rich phase converted to cloudy phase at a triple junction

with increasing temperature (up to 200 °C) and even reaches 27% and often turns into the cloudy phase. In the second path, which usually occurs at a temperature above 200 °C, the semi-spherical Nd-rich phase absorbs less oxygen, which is a sign of hydrogen absorption and the formation of neodymium hydride. Consequently, the morphology of the phase changes into a *cupcake* structure due to the induced expansion by the formation of NdH_2, as shown in Fig. 12. This morphology was not observed at temperatures below 200 °C, which contradicts the thermodynamics of neodymium hydride formation, as NdH_2 is more stable at room temperature [4], despite the claims made by various researchers [5, 21, 45, 46] about the formation of neodymium hydride after low-temperature hydrogenation and its higher stability based on the ΔG of hydride formation reactions [4], experimental evidence (e.g., X-ray diffraction) on the detection of NdH_x after hydrogenation is not readily accessible or valid. Also, Onel et al. [24] reported that there is no detectable NdH_x after hydrogenation at room temperature. The kinetics of the reaction can justify this contradiction with the thermodynamics of NdH_2 formation. The parameters that affect the kinetics of the reaction are the hydrogen pressure and flow rate, the holding time, the temperature or activation energy, and the interfacial reaction between the surface layer and the substrate for the penetration of hydrogen into the bulk of the magnet [20, 21, 47–50]. Pressure, flow rate, and holding time were set so that only the effects of temperature could be observed. Still, the value of these parameters was chosen in accordance with other studies [20, 21, 36, 45, 51] to ensure that the reactions were completed. Higher pressure

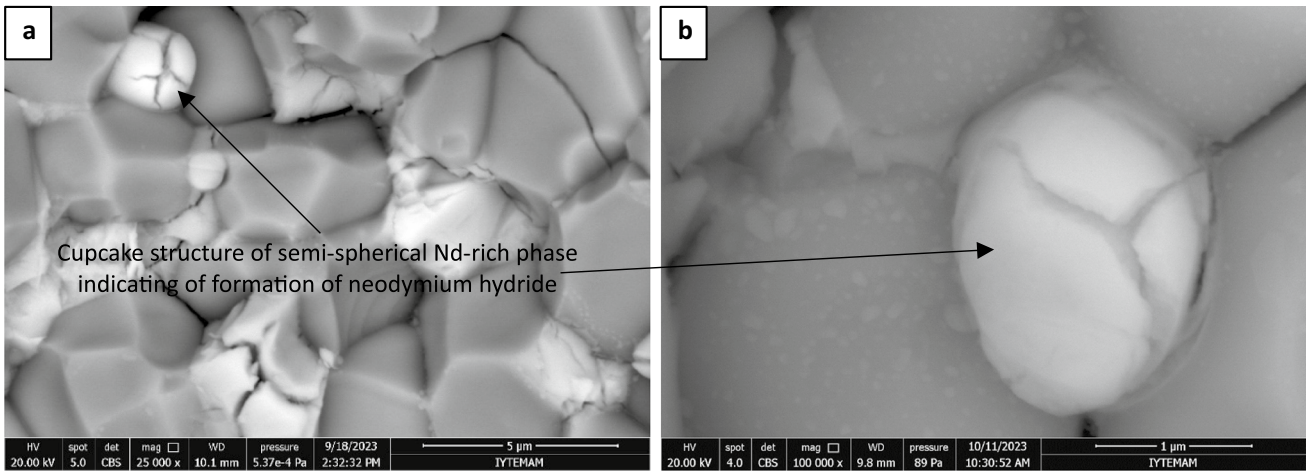

Fig. 12 BSE-SEM images of the semi-spherical Nd-rich phase with a cupcake morphology indicating the formation of NdH_2 after hydrogenation at **a** 350 °C, and **b** 400 °C

Table 6 Average chemical composition (wt.%) of semi-spherical Nd-rich phase before and after low-temperature hydrogenation of NdFeB magnets, obtained by EDS point analysis

Elements	Before HD	HD at 25 °C	HD at 100 °C	HD at 200 °C	HD at 400 °C
O	9.43 ± 4.79	15.39	17.30 ± 9.88	10.20 ± 9.35	9.99 ± 8.73
Fe	13.92 ± 6.13	10.17	17.70 ± 5.45	16.12 ± 8.94	12.26 ± 6.02
Pr	16.45 ± 3.98	14.13	11.64 ± 2.81	13.77 ± 2.87	14.24 ± 0.81
Nd	60.21 ± 5.97	59.89	53.26 ± 5.7	59.77 ± 11.08	63.48 ± 5.23

can indeed lead to the formation of NdH_3 [52]. The diffusion step controls the reaction rate at temperatures below 100 °C, while the interface between the reacted region and the bulk of the Nd-rich phase controls the rate at temperatures above 100 °C. As the temperature increases, the kinetic energy and mobility of hydrogen atoms significantly rise. This elevated mobility allows hydrogen atoms to effectively overcome the surface energy barrier that initially impedes their entry into the bulk of NdFeB magnets. As a result, the higher temperature not only accelerates the rate of hydrogen absorption but also promotes a more extensive and uniform formation of NdH_2 [40, 41, 45, 53, 54].

Table 6 shows the EDS point analysis of the average chemical composition of the semi-spherical Nd-rich phase at different hydrogenation temperatures. While the EDS results for a hydrogenation temperature of 400 °C were all from a semi-spherical Nd-rich phase with a cupcake structure, the result for a hydrogenation temperature of 200 °C was a mixture of standard and cupcake structures. The similar amount of oxygen after hydrogenation at 400 °C as before HD (see Table 6) could be due to the magnets being exposed to air for a longer time before HD, as the Nd-rich phase is very reactive. Therefore, based on the report of Mo et al. [26], the crystal structure of the semi-spherical Nd-rich phase with cupcake structure could be DHCP, while the standard structure with oxygen content above 9% is FCC structure and contains the neodymium oxide in the form of Nd_2O_3. The semi-spherical Nd-rich phase (labeled in Fig. 8), which is located at the triple junctions and has an average size of 4 µm, contains about 80% Nd and Pr, 20% Fe, and can take up about 10% oxygen before hydrogenation.

Conclusion

The microstructural investigation of the phase transformations of the NdFeB magnets was carried out before and after low-temperature hydrogenation in the range of 25 to 400 °C. The NdFeB magnets consist of two main phases, including the matrix grain of $Nd_2Fe_{14}B$ and the Nd-rich phase.

The Nd-rich phase was observed in various morphologies and chemical compositions, including spherical particles, referred to as the *spherical Nd-rich phase*, and the grain boundary network. The grain boundary network consists of a thin Nd-rich layer between the matrix grains and accumulated Nd at the triple junctions of the matrix grains, referred to as the *semi-spherical Nd-rich phase*. The spherical Nd-rich phase is located on the surface of the matrix grains, which does not undergo any visible changes during the hydrogenation process up to 400 °C. Most of the Nd-rich phase formed a thin grain boundary phase network isolating the matrix grain; however, Nd was already accumulated at the triple junctions of the matrix grain before hydrogenation.

After the hydrogenation process, four different hydrides ($Nd_2Fe_{14}BH_{1.04}$, $Nd_2Fe_{14}BH_{1.86}$, $Nd_2Fe_{14}BH_{3.31}$, $Nd_2Fe_{14}BH_{4.73}$) with different hydrogen content were observed. The hydrogen index (x in $Nd_2Fe_{14}BH_x$) increased from room temperature to 100 °C due to the increasing diffusivity, and the index decreased when the temperature increased to 400 °C, mainly due to the interfacial barrier and the shorter residence time of hydrogen atoms in the interstitial sites.

During hydrogenation, most of the Nd-rich thin grain boundary phase absorbs oxygen and transforms into an Nd-rich cloudy phase. The semi-spherical Nd-rich phase mainly forms neodymium oxide at a hydrogenation temperature below 200 °C and hydride at a hydrogenation temperature above 200 °C. The formation of hydride is accompanied by the formation of a cupcake structure and local expansion. The oxygen uptake of all Nd-rich phases initially increases with increasing hydrogenation temperature up to 300 °C, and then it decreases due to the formation of neodymium hydride, a phase stable against oxidation.

The finest particle size is reached when the hydrogen index is at its highest. At higher temperatures, long transgranular cracks occurred, leading to the cutting of the grains, thus, breaking the bulk and releasing the energy of the system before the formation of high index hydride, thus, resulting in a lower degree of pulverization.

Acknowledgements This research was funded by the Scientific and Technological Research Council of Türkiye (TÜBITAK) under the BIDEB-2232 program with grant number 118C311. Center for Materials Research at İzmir Institute of Technology is gratefully acknowledged for the sample analyses. Environmental Research Center at İzmir Institute of Technology is gratefully acknowledged for metal analyses. The authors gratefully acknowledged the support from Exitcom Recycling Company for providing all needed samples.

Funding Open access funding provided by the Scientific and Technological Research Council of Türkiye (TÜBİTAK). Open access funding provided by the Scientific and Technological Research Council

of Türkiye (TÜBİTAK). This research was funded by the Scientific and Technological Research Council of Turkey (TÜBITAK) under the BIDEB-2232 program with grant number 118C311.

Declarations

Conflict of interest The authors declare that they have no conflict of interest.

References

1. Sagawa M et al (1984) Permanent magnet materials based on the rare earth-iron-boron tetragonal compounds. IEEE Trans Magn 20(5):1584–1589
2. Vial F et al (2002) Improvement of coercivity of sintered NdFeB permanent magnets by heat treatment. J Magn Magn Mater 242:1329–1334
3. Herbst JF et al (1984) Relationships between crystal structure and magnetic properties in Nd 2 Fe 14 B. Phys Rev B 29(7):4176
4. Habibzadeh A, Kucuker MA, Gökelma M (2023) Review on the parameters of recycling NdFeB magnets via a hydrogenation process. ACS Omega. https://doi.org/10.1021/acsomega.3c00299
5. Prokofev PA et al (2020) Blending powder process for recycling sintered Nd-Fe-B magnets. Materials 13(14):3049
6. Rong C, Shen B (2018) Nanocrystalline and nanocomposite permanent magnets by melt spinning technique. Chin Phys B 27(11):117502
7. Lucas J et al (2014) Rare earths: science, technology, production and use. Elsevier, Amsterdam
8. Koyama T, Tsukada Y, Abe T (2021) Computational thermodynamics and microstructure simulations to understand the role of grain boundary phase in Nd-Fe-B hard magnets. Sci Technol Adv Mater 22(1):1–13
9. Lv M et al (2021) Progress on modification of microstructures and magnetic properties of Nd-Fe-B magnets by the grain boundary diffusion engineering. J Magn Magn Mater 517:167278
10. Zhou T et al (2021) Sintered NdFeB magnets with Tb-Dy double-layer core/shell structure were fabricated by double alloy method and grain boundary diffusion. J Alloy Compd 856:158191
11. Zhou B, Li Z, Chen C (2017) Global potential of rare earth resources and rare earth demand from clean technologies. Minerals 7(11):203
12. Buschow K (1997) Magnetism and processing of permanent magnet materials. Handb Magn Mater 10:463–593
13. Binnemans K et al (2013) Recycling of rare earths: a critical review. J Clean Prod 51:1–22
14. Europeia C (2020) Communication from the commission to the european parliament, the council, the european economic and social committee and the committee of the regions critical raw materials resilience: charting a path towards greater security and sustainability. European Commission: Brussels, Belgium
15. Wübbeke J (2013) Rare earth elements in China: policies and narratives of reinventing an industry. Resour Policy 38(3):384–394
16. Dushyantha N et al (2020) The story of rare earth elements (REEs): occurrences, global distribution, genesis, geology, mineralogy and global production. Ore Geol Rev 122:103521
17. Yang Y et al (2017) REE recovery from end-of-life NdFeB permanent magnet scrap: a critical review. J Sustain Metall 3:122–149
18. Karal E et al (2021) Hydrometallurgical recovery of neodymium from spent hard disk magnets: a life cycle perspective. J Clean Prod 288:125087
19. Walton A et al (2015) The use of hydrogen to separate and recycle neodymium–iron–boron-type magnets from electronic waste. J Clean Prod 104:236–241
20. Piotrowicz A et al (2020) The use of thermal hydrogen decrepitation to recycle Nd–Fe–B magnets from electronic waste. J Min Metall Sect B 56(3):415–424
21. Michalski B et al (2022) Experimental evidence for the suitability of the hydrogen decomposition process for the recycling of Nd–Fe–B sintered magnets. J Magn Magn Mater 548:168979
22. Isnard O et al (1995) Neutron-diffraction study of the insertion scheme of hydrogen in Nd2Fe14B. J Appl Phys 78(3):1892–1898
23. Ram S et al (1997) Formation of Nd 2 Fe 14 B hydride by milling of anhydride particles in toluene in a closed reactor. Bull Mater Sci 20:1049–1058
24. Önal MAR et al (2017) Comparative oxidation behavior of Nd-Fe-B magnets for potential recycling methods: effect of hydrogenation pre-treatment and magnet composition. J Alloy Compd 728:727–738
25. Sepehri-Amin H, Hirosawa S, Hono K (2018) Advances in Nd–Fe–B based permanent magnets, In: Handbook of magnetic materials. Elsevier, pp 269–372
26. Mo W et al (2008) Dependence of the crystal structure of the Nd-rich phase on oxygen content in an Nd–Fe–B sintered magnet. Scripta Mater 59(2):179–182
27. Tang W et al (1988) An investigation of the Nd-rich phases in the Nd-Fe-B system. J Appl Phys 64(10):5516–5518
28. Wang G et al (2019) Mechanical properties and the composition of Nd-rich phase in sintered Nd–Fe–B magnets prepared by spark plasma sintering. J Magn Magn Mater 486:165261
29. Xin F et al (2013) Microstructural investigation of Nd-rich phase in sintered Nd–Fe–B magnets through electron microscopy. J Rare Earths 31(8):765–771
30. Li W, Ohkubo T, Hono K (2009) Effect of post-sinter annealing on the coercivity and microstructure of Nd–Fe–B permanent magnets. Acta Mater 57(5):1337–1346
31. Sepehri-Amin H et al (2012) Grain boundary and interface chemistry of an Nd–Fe–B-based sintered magnet. Acta Mater 60(3):819–830
32. Sasaki T, Ohkubo T, Hono K (2016) Structure and chemical compositions of the grain boundary phase in Nd–Fe–B sintered magnets. Acta Mater 115:269–277
33. Shinba Y et al (2005) Transmission electron microscopy study on Nd-rich phase and grain boundary structure of Nd–Fe–B sintered magnets. J Appl Phys. https://doi.org/10.1063/1.1851017
34. Yin X, Jones I, Harris I (1993) The microstructural characterisation of Nd–Fe–B alloys II: microstructural investigation of cast Nd–Fe–B materials. J Magn Magn Mater 125(1):91–102
35. Wang S, Li Y (2005) In situ TEM study of Nd-rich phase in NdFeB magnet. J Magn Magn Mater 285(1–2):177–182
36. Zakotnik M, Harris I, Williams A (2009) Multiple recycling of NdFeB-type sintered magnets. J Alloy Compd 469(1–2):314–321

37. Turnbull A (2012) Hydrogen diffusion and trapping in metals. Gaseous hydrogen embrittlement of materials in energy technologies. Elsevier, pp 89–128
38. Hara S et al (2012) Hydrogen diffusion coefficient and mobility in palladium as a function of equilibrium pressure evaluated by permeation measurement. J Membr Sci 421:355–360
39. Wirth S, Skomski R, Coey J (1997) Hydrogen in R 2 Fe 17 intermetallic compounds: structural, thermodynamic, and magnetic properties. Phys Rev B 55(9):5700
40. Wipf H (1997) Hydrogen in metals III: properties and applications. Springer, New York
41. Volkl J, Alefeld G (2005) Diffusion of hydrogen in metals. In: Hydrogen in metals I: basic properties. Springer, Berlin, pp 321–348
42. Kilner JA et al (2012) Functional materials for sustainable energy applications. Elsevier, Amsterdam
43. Meng R-Y et al (2023) Thermal expansion behavior of sintered Nd–Fe–B magnets with different Co contents and orientations. Chin Phys B 32(5):056501
44. Barson F, Legvold S, Spedding FH (1957) Thermal expansion of rare earth metals. Phys Rev 105(2):418
45. Li X et al (2019) Effect of hydrogen pressure on hydrogen absorption of waste Nd–Fe–B sintered magnets. J Magn Magn Mater 473:144–147
46. Li C et al (2015) Recycling of scrap sintered Nd–Fe–B magnets as anisotropic bonded magnets via hydrogen decrepitation process. J Mater Cycles Waste Manage 17(3):547–552
47. Turek K, Liszkowski P, Figiel H (2000) The influence of the kinetics of the hydrogenation of Nd–Fe–B alloys on hydrogen distribution in the alloy phases. J Alloy Compd 309(1–2):239–243
48. Luo J et al (2011) Hydrogen absorption and desorption characteristics of high coercivity NdDyFeCoNbCuB sintered magnet. I. Low temperature hydrogen decrepitation treatments. J Alloys Compd 509(11):4252–4259
49. Sarussi D et al (1993) The kinetics and mechanism of cerium hydride formation. J Alloy Compd 191(1):91–99
50. Bloch J, Hadari Z, Mintz MH (1984) The topochemistry of hydride formation in rare earth metals. J Less Common Metals 102(2):311–328
51. Zakotnik M, Harris I, Williams A (2008) Possible methods of recycling NdFeB-type sintered magnets using the HD/degassing process. J Alloy Compd 450(1–2):525–531
52. Zhou D et al (2020) High-pressure synthesis of magnetic neodymium polyhydrides. J Am Chem Soc 142(6):2803–2811
53. Sanchez J et al (2008) Hydrogen in α-iron: stress and diffusion. Phys Rev B 78(1):014113
54. Vajda P (1995) Hydrogen in rare-earth metals, including RH2+x phases. Handb Phys Chem Rare Earths 20:207–291